g factor of topological interface states in $Pb_{1-x}Sn_xSe$ quantum wells

Jiashu Wang [1,*] Xinyu Liu [1] Tianyi Wang [1] Mykhaylo Ozerov,[2] and Badih A. Assaf [1]
[1]*Department of Physics and Astronomy, University of Notre Dame, Notre Dame, Indiana 46556, USA*
[2]*National High Magnetic Fields Laboratory, Florida State University, Tallahassee, Florida 32310, USA*

(Received 8 December 2022; revised 27 March 2023; accepted 14 April 2023; published 28 April 2023)

Topological crystalline insulators from the $Pb_{1-x}Sn_xSe$ family host textbook Dirac surface states that are nearly electron-hole symmetric and isotropic in momentum space. The high mobility of charge carriers possible in these materials allows one to reach the quantum limit at reasonably achievable magnetic fields. We exploit this advantage to combine magnetooptical Landau level spectroscopy, Shubnikov–de Haas transport measurement, and consistent modeling of the two experiments to precisely extract the band parameters of the topological states of this system along with their *g* factor. We find an enhanced *g* factor with field dependence compared with bulk states. This information is vital to the realization and understanding of novel quantized Hall effect, stemming from the mirror protected valley-degenerate Dirac states of this material family.

DOI: 10.1103/PhysRevB.107.155307

I. INTRODUCTION

Topological crystalline insulators (TCIs) are a class of topological matter in which crystalline symmetry combines with time-reversal symmetry to ensure the existence of gapless surface states. IV-VI materials, including $Pb_{1-x}Sn_xSe$ and $Pb_{1-x}Sn_xTe$, have been identified as TCIs [1–3]. They have a simple rocksalt structure and host four Dirac cones along the [111] surface. This valley degeneracy can lead to novel quantum phenomena such as a quantum anomalous Hall effect with high Chern number and an interaction-induced quantum Hall nematic state [4–6].

The electronic properties of bulk $Pb_{1-x}Sn_xSe$ have been explored by various techniques, such as magnetotransport [7–9], magneto-optics [10,11], and angle-resolved photoemission spectroscopy [3,12]. Magnetotransport has been commonly used to study IV-VI materials, as the TCI properties can be reflected by the weak antilocalization effect and Shubnikov–de Haas oscillations [13,14]. However, most transport measurements fail to produce a complete electronic structure of the surface states, mostly due to the contribution from bulk conducting channels. Extracting the *g* factor and Zeeman splitting is particularly challenging without independent knowledge of where the Fermi level is and an independent indexing of the quantum oscillations. Notably, the *g* factor of the surface states of TCIs has not yet been measured. There have been attempts to extract it using scanning tunneling spectroscopy measurements and quantum oscillations in Bi-based TIs. Values as high as 50 were recovered from the behavior of the $N = 0$ Landau level in $Bi_2(Te, Se)_3$ [15], while quantum oscillations yielded inconsistent results [16–19]. This inconsistency is not an uncommon issue, as the g factor is known to be field and energy dependent for systems with nonparabolic dispersions, resulting from strong spin-orbit interactions [20].

In our previous work [13], we have successfully grown $Pb_{0.73}Sn_{0.27}Se$ quantum wells with high mobility and low carrier density. We studied their quantum coherent transport at low magnetic field. In this work, we perform high-field magnetotransport and magnetooptical measurements on the quantum wells to extract consistent band information valuable to realize and understand the quantum Hall effects predicted in this material system [2,4]. These parameters include the *g* factor. We observed nonperiodic quantum oscillations in the magnetoresistivity between 3 and 16 T which are difficult to interpret without other experimental input. By employing magnetooptical Landau level spectroscopy, we extract the band parameters and model the Landau level dispersion versus magnetic field which allows us to reliably index observed oscillations. We find an excellent agreement between magnetotransport and magneto-optical measurement for a specific value of spin splitting. The crossing of Landau levels with the Fermi level allows us to model the quantum oscillations and extract the hole g factor of the topological interface states of $Pb_{0.73}Sn_{0.27}Se$ quantum wells.

II. EXPERIMENT

A. Sample structure

The sample structure is shown in Fig. 1(a). A 1-μm $Pb_{0.80}Eu_{0.20}Se$ layer and a PbSe/EuSe superlattice with a total thickness equal to 500 nm are grown as buffer layers on the BaF_2 [111] substrate. Then, the $Pb_{0.73}Sn_{0.27}Se$ quantum well is grown between a 40-nm $Pb_{0.80}Eu_{0.20}Se$ bottom barrier and a 50-nm $Pb_{0.80}Eu_{0.20}Se$ top barrier. A Sn content of $x = 0.3$ is chosen to realize an inverted bulk gap close to 100 meV and an isotropic bulk Fermi surface [11]. Under the latter condition, the four Dirac surface states of the material become isotropic and identical, thus removing the ambiguity related to valley degeneracy [11,14]. The well is encapsulated between two identical $Pb_{0.80}Eu_{0.20}Se$ barriers, which limits top-bottom asymmetry. The Sn concentration, layer thickness, and strain characteristics are characterized by x-ray diffraction (XRD) and transmission electron microscopy (TEM), shown in our

*Corresponding author: jwang39@nd.edu

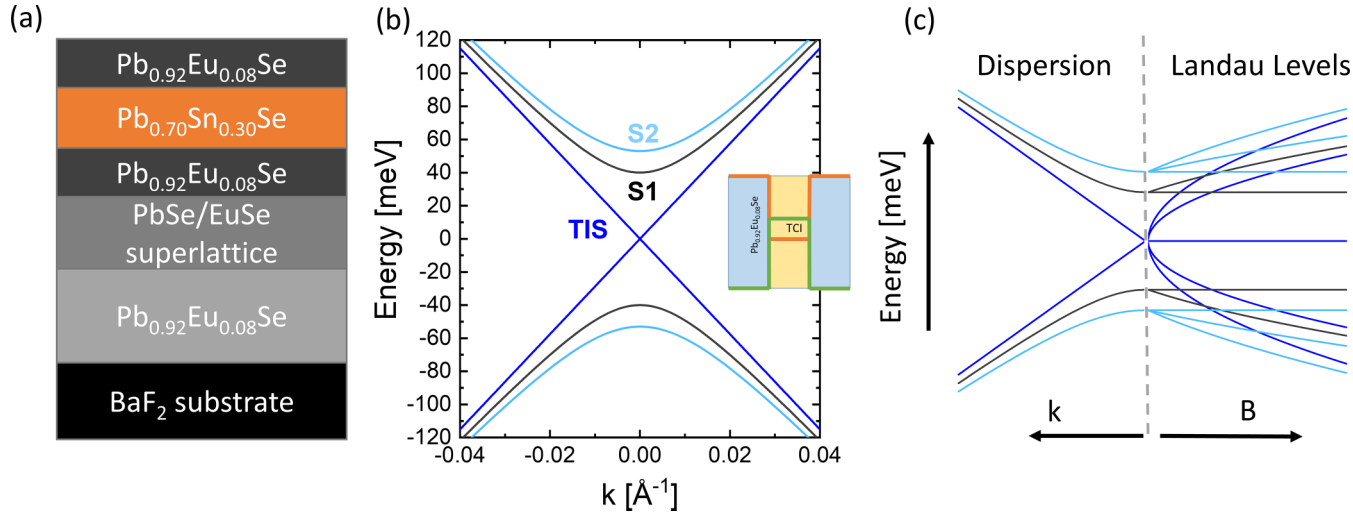

FIG. 1. (a) Structure of the quantum well. The well thickness is 50 nm and barrier thickness is 40 nm. (b) Band dispersion of TIS and "bulk" subbands S1 and S2. The inset diagram shows the inverted band alignment of the quantum well. (c) Landau levels of each band. Spin splitting is not included in this plot.

previous work [13]. Here we will focus our analysis on a single 50-nm quantum well.

The inverted band structure will lead to an evanescent gapless state at the interface that is topologically protected, together with gapped subbands originating from the quantum confinement of bulk states, as shown in Fig. 1(b). Each band has a separate Landau level (LL) fan illustrated in Fig. 1(c) in the presence of a magnetic field along the growth axis. The gaps, band dispersions, and LLs for each subband including the topological interface states (TISs) can be derived by combining the $k \cdot p$ model for IV-VI semiconductors and the envelope function approach, as shown in Refs. [11,13,21,22] and Appendix B. Here, a far-band correction, which consists of an orbital component and a spin component, is expressed as $\hbar\tilde{\omega}$. Its origin is discussed in detail in Appendix C, following a similar treatment previously carried out for the bulk band structure [7,23], The LLs in the conduction (written as E) and valence band (written as H) are expressed as

$$E_i^{N,(\uparrow,\downarrow)} = \pm\hbar\tilde{\omega}_{\rm eff} + \sqrt{(\Delta_{\rm i} - N\hbar\tilde{\omega}_{\rm eff})^2 + 2e\hbar N v_c^2 B},$$
$$H_i^{N,(\uparrow,\downarrow)} = \pm\hbar\tilde{\omega}_{\rm eff} - \sqrt{(\Delta_{\rm i} - N\hbar\tilde{\omega}_{\rm eff})^2 + 2e\hbar N v_c^2 B}, \quad (1)$$

where Δ_i is the band edge position of each subband, i is the subband index ($i = 0$ and $\Delta_0 \to 0$ meV for TIS), N denotes the LL index redefined according to Refs. [10,24] (for details see Appendix B), v_c is the band velocity related to the $k \cdot p$ interband matrix element, and $\tilde{\omega}_{\rm eff} = \frac{eB}{\tilde{m}_{\rm eff}}$ represents the far-band contributions to the effective mass $\tilde{m}_{\rm eff}$. Its meaning and origin are discussed in detail in Appendix C. This contribution gives a small parabolic correction to the linear dispersion of the interface states. We are also using the approximation that $\tilde{g}_{\rm eff}\mu_B B \approx -\hbar\tilde{\omega}_{\rm eff}$, which has been used in previous works [7,23,25,26], where $\tilde{g}_{\rm eff}$ is the far-band correction to the g factor. Although such an approximation was originally used for bulk states [7], we show that it applies to surface states as well in Appendix C. Regardless of the accuracy of this assumption, the far-band orbital and spin Zeeman parts cannot be easily distinguished using measurements in the geometry that we have chosen in this work. Our objective will be to determine their overall impact on the Landau levels, essentially consisting of a pseudospin splitting. Notice here that only the far-band correction to the g factor appears in the expression for the Landau levels. We discuss in detail later how it relates to the total g factor. In what comes next, we determine the experimental values of $\Delta_{\rm i}$, v_c, and $\tilde{m}_{\rm eff}$ by combining magneto-optical and magnetotransport measurements.

B. Magneto-optical Landau level spectroscopy of the band structure of topological states

We have performed magnetooptical infrared spectroscopy to extract the band parameters that appear in Eq. (1) at 5.5 K using an applied magnetic field up to 17.5 T in the Faraday geometry. In the presence of the magnetic field, the incident infrared electromagnetic wave excites transitions between different LLs, given dipole selection rules that conserve pseudospin and obey parity rules (transitions between N and $N \pm 1$), as shown in Fig. 2(a). Arrows represent transitions between LLs originating from either the TIS or S1 band. According to the selection rules, the optically active interband transitions occur between H_i^N and $E_i^{N\pm1}$ Landau levels for electrons with same spin [27–30]. From Eq. (1) we can derive

$$\Delta E = E_i^{N\pm1} - H_i^N = \sqrt{[\Delta_{\rm i} - (N \pm 1)\hbar\tilde{\omega}_{\rm eff}]^2 + 2e\hbar N v_c^2 B} + \sqrt{(\Delta_{\rm i} - N\hbar\tilde{\omega}_{\rm eff})^2 + 2e\hbar N v_c^2 B}. \quad (2)$$

The experimental relative transmission spectra $T(B)/T(0)$ at each field are shown in Fig. 2(b). The minima in the relative spectra, which shift to a higher energy as the field increases, represent the transition between LLs. In Fig. 2(c) the energy of each minimum is plotted versus magnetic field as points. We identify the origin of these transmission minima by fitting with Eq. (2). Transitions from the same subband are in the

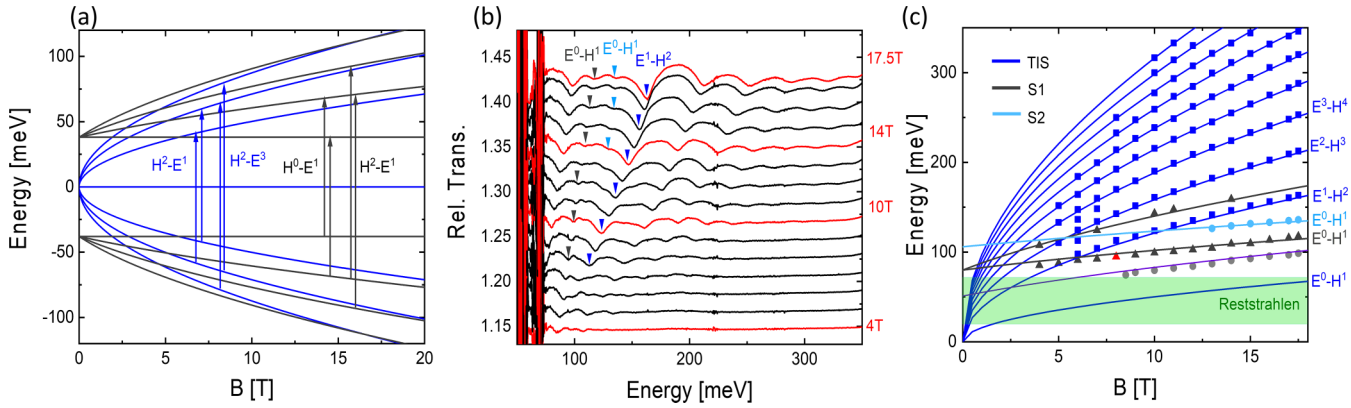

FIG. 2. (a) Landau levels of TIS and S1. Arrows represent electron transitions between LLs of the same band. To make the transition clearer to understand, the Zeeman splitting term ($\pm\hbar\tilde{\omega}_{\rm eff}$) is not included in the plot. (b) Relative magneto-optical spectra [$T(B)/T(0)$] on S1 between 4 and 17.5 T, measured at 5.5 K. Transitions are marked with different color that is consistent with (c). (c) Fan chart extracted from spectra. All points represent the minima in (a) and lines are fit using Eq. (2). In the green region below ∼70 meV, the signal is blocked due to the reststrahlen band of BaF_2 and absorption through a ZnSe window used in the experiment.

same color. The deep blue lines represent transitions from the LLs of the TIS, the grey and light blue lines represent transitions from S1 and S2, respectively. An additional purple line represents hybrid intersubband transitions. A detailed discussion of this transition is beyond the scope of this work. From the fit, we can get an estimation of the band parameters including the band gap 2Δ, the band velocity v_c related to the $k\cdot p$ matrix element, and the far-band effective mass correction $\tilde{m}_{\rm eff}$. A sufficient number of points from lower-index LL transitions give a precise fit and a precise value of the band gap Δ_i. The fitting result matches well with experimental data for the parameters shown in Table I.

The far-band correction to the effective mass cannot however be extracted reliably by this method, as it does not influence the LL transitions dramatically. We will show next that by combining the results of our magnetooptical Landau level spectroscopy with Shubnikov–de Haas measurements, this precision can be dramatically improved.

C. Spin splitting from Shubnikov–de Haas measurements

Electrical magnetotransport measurements are performed between 1.5 and 20 K using the standard five-probe method, with magnetic field up to 16 T. The result is shown in Fig. 3. Figure 3(a) shows the longitudinal resistance $R_{\rm xx}$ versus magnetic field. Although $R_{\rm xx}$ is quasilinear, we can observe small oscillations emerging at high magnetic field. By performing a linear fit, we extract this small change $\Delta R_{xx} = R_{xx} - R_{fit}$, as shown in Fig. 3(b) for different temperatures. The recovered signal exhibits Shubnikov–de Haas oscillations, which relate to the crossings between the Fermi level and Landau levels. At each crossing, the carriers are delocalized, leading to an increase of the conductivity σ_{xx}. However, whether $R_{xx} \sim \frac{\sigma_{xx}}{\sigma_{xx}^2+\sigma_{xy}^2}$ behaves as a minimum or maximum when σ_{xx} is maximum depends on the scale of σ_{xx} and σ_{xy} [31]. In our case, σ_{xy} is larger when the field is above 5 T, leading to a maximum of R_{xx} when σ_{xx} goes to a maximum. The value of $\sigma_{\rm xy}$, σ_{xx} is calculated by the Drude model and shown in Fig. 3(c).

TABLE I. Fitting parameters of sample S1 from transmission spectra. m_e is the free electron mass.

	TIS	S1	S2
$\Delta_{\rm i}$ from experiment (meV)	0(+5)	40(±3)	53(±5)
Δ_i from calculations (meV)	0	38	49
v_c		$(4.36\pm0.10)\times10^5$ m/s	
$\lvert\tilde{m}_{\rm eff}\rvert/m_e$		0.30(±0.15)	

The oscillating signal is aperiodic and yields only four oscillation maxima making it difficult to analyze without direct recourse to a fan chart. The field at which the oscillation maxima occur are extracted and are indicated by arrows in Fig. 3(d), where we also plot the LLs of the TIS, S1, and S2 (including Zeeman splitting) with parameters fitted from magneto-optics. The dashed line represents the Fermi level, which crosses the valence band. It can be estimated from where the LL transition disappears. For example, the $E_0^2 - H_0^3$ disappear between 3.5 and 4 T [Fig. 2(c)], meaning the H_0^3 LLs just go across the Fermi level in that field range. By comparing several transitions, we can estimate the Fermi level to be -55 ± 5 meV (negative because the sample is p type).

III. DISCUSSION

The crossings deduced from Shubnikov–de Haas oscillations, and the predicted crossings from magneto-optical measurement, can be made to match well by further constraining the far-band corrections related to $\tilde{m}_{\rm eff}/m_0$ as shown in Fig. 3(d). The two crossings at higher field are of particular importance, as they originate from spin-up and spin-down Landau levels with the same index $N=1$. From Eq. (1) we can derive that the distance between these two crossings is

$$\Delta\left(\frac{1}{B_{{\rm TIS},N=1}}\right) = \frac{1}{B^{\uparrow}_{{\rm TIS},N=1}} - \frac{1}{B^{\downarrow}_{{\rm TIS},N=1}} = \frac{4e\hbar E_f}{\tilde{m}_{\rm eff}\left(E_f^2-\Delta^2\right)}, \tag{3}$$

where $B^{\uparrow}_{{\rm TIS},N=1}$, $B^{\downarrow}_{{\rm TIS},N=1}$ are the crossings between the Fermi level and $H_0^{1,\uparrow}$, $H_0^{1,\downarrow}$. Thus, after finer tuning of the param-

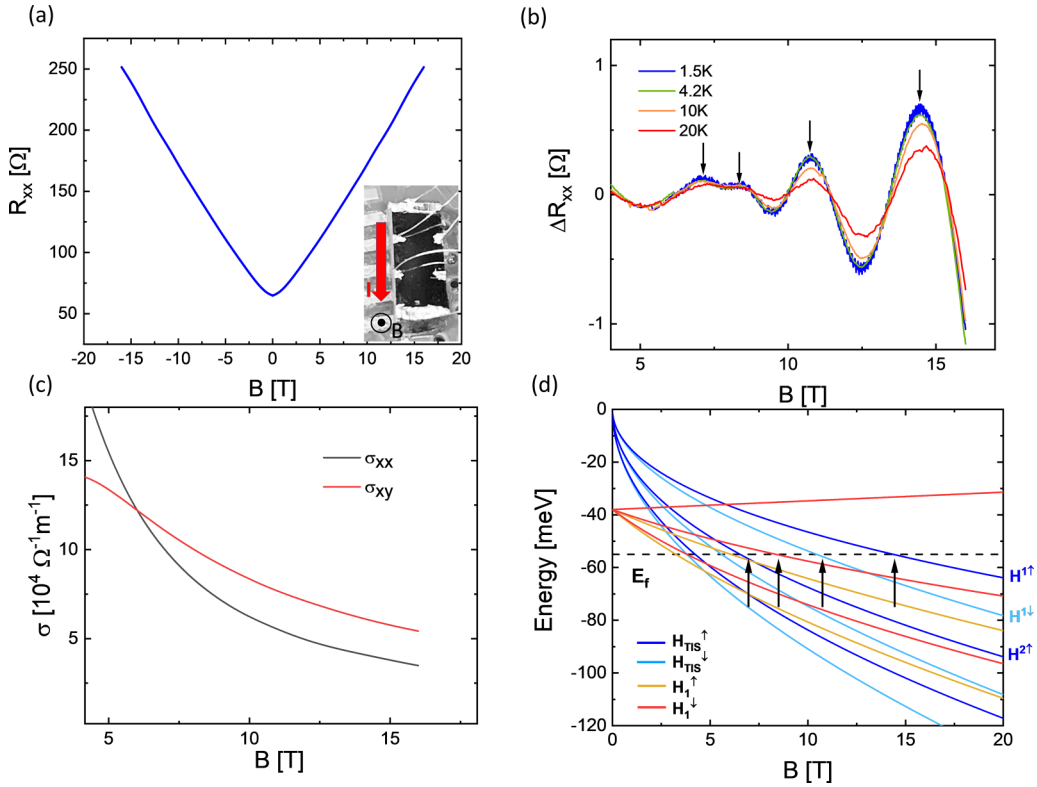

FIG. 3. Transport measurement of the sample. (a) R_{xx} measured at 1.5 K. Weak oscillations can be observed at high field. Inset: photograph of the sample setup for transport. (b) ΔR_{xx} extracted by a linear fit. The peaks of the oscillations are indicated by black arrows. (c) Longitudinal and transverse conductance σ_{xx}, σ_{xy} calculated from Drude model. (d) Landau levels of TIS and S1. Black arrows are in the same position with (b).

eters to match all four crossings, the band edge correction to the effective mass $\tilde{m}_{\text{eff}}$ can be more precisely derived to be $\frac{\tilde{m}_{\text{eff}}}{m_e} = 0.32 \pm 0.02$. The uncertainty is mostly due to the uncertainty on the position of the Fermi level. It is in the range of the previous reports on bulk epilayers of IV-VI materials [10,11,24]. The corresponding far-band g factor is $\tilde{g}_{\text{eff}} \approx \frac{2m_e}{\tilde{m}_{\text{eff}}} = 6.2 \pm 0.1$. We highlight here that $\tilde{g}_{\text{eff}}$ is the effective far-band correction to the g factor and not the overall effective g factor. The splitting seen in Fig. 3(d) originates from spin-up and spin-down states that are originally Kramers' partners without magnetic field (Appendix D). The breaking of time-reversal symmetry under a magnetic field causes this splitting. The overall effective g factor "g" of the system can be found by extracting the spin-splitting energy between Landau levels (with redefined index) from the fan chart in Fig. 3(d).

The $k \cdot p$ treatment used above simplifies the Landau levels of TCIs by introducing an index change, explained in Appendix A. The overall effective g factor should use the original Landau index n of Mitchell and Wallis [29] (discussed in Appendix A) which describes the true spin splitting between states of identical Landau index. It is found to be consistent with spin resonance measurements in bulk [32,33], and is systematically used to characterize the spin splitting of non-parabolic systems [14,16,34]:

$$g(n) = \frac{H(n,\uparrow) - H(n,\downarrow)}{\mu_B B}(n \geqslant 0) = \frac{H(N,\uparrow) - H(N+1,\downarrow)}{\mu_B B}(N \geqslant 0). \quad (2)$$

It can be seen from Eq. (1) that the g is dependent on both the index N and the magnetic field B. This is not unusual for materials with nonparabolic band dispersions, and should also hold for topological surface states. The calculated result for the surface state is shown in Fig. 4(a). The parameters used for calculation are taken explicitly from our magneto-optical and magnetotransport results, as discussed earlier. In a reasonable field range for measurements (2–20 T), the g factor for $n = 1$ and $n = 2$ exceeds 100 below 2 T. For the high-n limit, the g factor is close to 20 between 5 and 20 T.

The effective g factor we get for the interface states is enhanced compared with the reported value in bulk $Pb_{1-x}Sn_xSe$ (30–70) [14,35,36]. Such an enhancement of the surface state g factor compared with bulk are reported in other systems, too [16,34,37]. In our case, this can be understood from the conventional Roth formula [38], where a smaller gap leads to an enhanced g. On the other hand, the calculated g factor for the first subband S1 as shown in Fig. 4(b) agrees with bulk values. The field dependence of the g factor can be explained by the strong mixing between orbital and spin degrees of freedom in IV-VI materials. Such behavior is also observed in other systems with strong spin-orbit coupling such as InAs [39] and HgTe [40].

In summary, we have performed magneto-optical Landau level spectroscopy and Shubnikov–de Haas oscillation measurements on high-mobility $Pb_{0.73}Sn_{0.27}Se$ topological quantum wells. The Shubnikov–de Haas oscillations and the magnetooptical spectra are consistent with each other. By

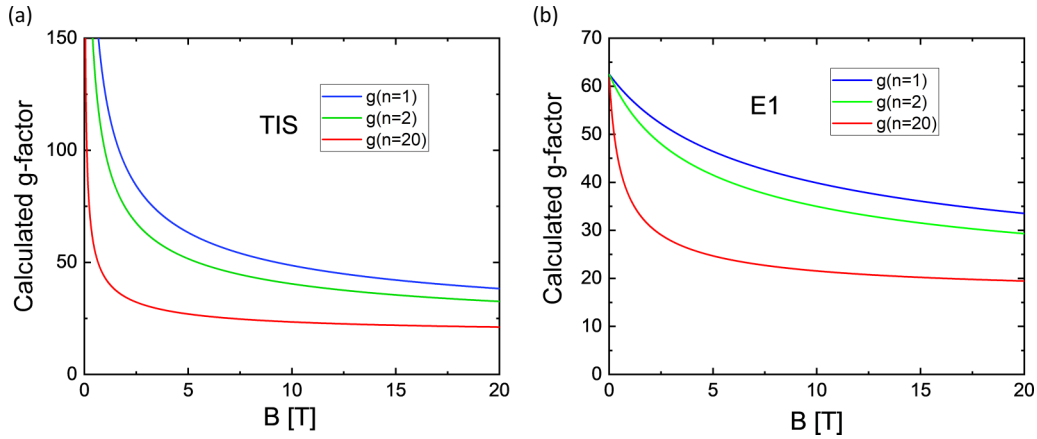

FIG. 4. Calculated effective g factor defined in Eq. (2) for (a) topological surface states and (b) the first subband S1, which depends on the Landau index n. We choose to show the case of $n = 1$, 2 and a large limit $n = 20$.

combining the two techniques, we are able to get well-constrained band parameters including the far-band correction to the effective mass and g factor, which is extracted from the spin splitting of Shubnikov–de Haas peaks. The recovered effective g factor g of the topological surface state is enhanced compared with bulk states. This effective g factor accounts for the splitting between Landau levels of opposite pseudospin. It is dependent on the Landau index, the magnetic field, and the energy. Finally, the existence of quantum oscillations is a promising signature to achieve the exotic quantized Hall effect predicted for the topological crystalline insulators.

ACKNOWLEDGMENTS

Work was supported by National Science Foundation Grant No. DMR-1905277. A portion of this work was performed at the National High Magnetic Field Laboratory, supported by National Science Foundation Cooperative Agreement No. DMR-1644779 and the State of Florida. The authors would like to thank D. Smirnov for the experiment support and useful discussions.

APPENDIX A: $k \cdot p$ HAMILTONIAN AND FAR-BAND APPROXIMATION OF BULK $Pb_{0.73}Sn_{0.27}Se$; REFINED LL INDEX

A $k \cdot p$ Hamiltonian was developed by Mitchell and Wallis to describe the $L_6^{\pm}$ band of lead salts. For [111] orientation in the nontrivial case, in the basis $L_{6\alpha}^{+}|n\rangle$, $L_{6\beta}^{+}|n+1\rangle$, $L_{6\alpha}^{-}|n\rangle$, $L_{6\beta}^{-}|n+1\rangle$, the Hamiltonian is written as follows:

$$\begin{pmatrix} \Delta - \left(n+\frac{1}{2}\right)\hbar\tilde{\omega}_c + \frac{1}{2}\tilde{g}_c\mu_B B & 0 & \hbar v_z k_z & \sqrt{2(n+1)\hbar e B v_c^2} \\ 0 & \Delta - \left(n+\frac{3}{2}\right)\hbar\tilde{\omega}_c - \frac{1}{2}\tilde{g}_c\mu_B B & \sqrt{2(n+1)\hbar e B v_c^2} & -\hbar v_z k_z \\ \hbar v_z k_z & \sqrt{2(n+1)\hbar e B v_c^2} & -\Delta - \left(n+\frac{1}{2}\right)\hbar\tilde{\omega}_v + \frac{1}{2}\tilde{g}_v\mu_B B & 0 \\ \sqrt{2(n+1)\hbar e B v_c^2} & -\hbar v_z k_z & 0 & -\Delta - \left(n+\frac{3}{2}\right)\hbar\tilde{\omega}_v - \frac{1}{2}\tilde{g}_v\mu_B B \end{pmatrix},$$

where $\tilde{\omega}_c$, $\tilde{\omega}_v$, $\tilde{g}_c$, $\tilde{g}_v$ are far-band contributions to the effective mass and g factor, separately. n is the true Landau level index. In the nontrivial case, L_6^+ is the conduction band and L_6^- is the valence band. α, β represent the pseudospin direction. $L_{6\alpha}^{+}$, $L_{6\beta}^{-}$ represents spin up; $L_{6\beta}^{+}$, $L_{6\alpha}^{-}$ represents spin down [29,41].

Far bands are nearly equally distant from the conduction and valence band. Thus, we can take $\tilde{\omega}_c \approx -\tilde{\omega}_v = \frac{eB}{\tilde{m}}$. Similarly, $\tilde{g}_c = -\tilde{g}_v = \tilde{g}$. Previous works have shown that for bulk PbSe, $|g\mu_B B| \approx |\hbar\omega|$ within the error. Since the far bands are close to 1 eV away from the $L_6^{\pm}$ bulk bands, we assume the approximation will not be affected by changing Sn concentration and still holds for $Pb_{0.73}Sn_{0.27}Se$. Nevertheless, $\hbar\omega$ and $g\mu_B B$ always bind together to affect the energy and we cannot distinguish them by Faraday geometry.

Solving the above Hamiltonian will get the energy values for nth Landau levels of bulk $Pb_{1-x}Sn_xSe$:

$$E_{L_{6\alpha}^{+},L_{6\beta}^{-}} = \pm\hbar\tilde{\omega} \pm \sqrt{[\Delta - (n+1)\hbar\tilde{\omega}]^2 + 2e\hbar v_c^2(n+1)},$$

$$E_{L_{6\beta}^{+},L_{6\alpha}^{-}} = \pm\hbar\tilde{\omega} \pm \sqrt{[\Delta - n\hbar\tilde{\omega}]^2 + 2e\hbar v_c^2 n}.$$

Thus, we can redefine an index N such that $N = n$ for $L_{6\beta}^{+}$ and $N = n+1$ for $L_{6\alpha}^{+}$; the same applies for L_6^- bands. Such change of index is shown in Fig. 5.

The selection rules for interband transitions has been discussed [27,28,30] and obey $\Delta n = 0$ or $\Delta n = \pm 2$ with same spin. In the refined N case, this is converted to $\Delta N = \pm 1$ with same spin direction. Transitions are plotted as green arrows in Fig. 5.

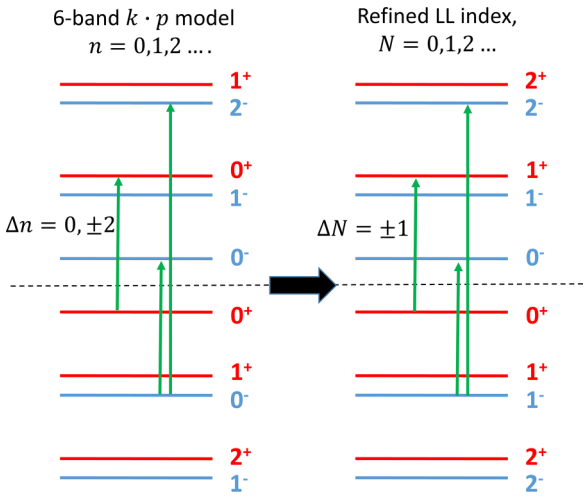

FIG. 5. Comparison between the original LL index n(left) from Refs. [10,29] and the refined LL index N (right) used in here and Refs. [7,11,23]. Green arrow represents interband transitions allowed by selection rules. For refined LL index, the transition happens between $\Delta N = \pm 1$ with same spin direction.

APPENDIX B: $k \cdot p$ ENVELOPE FUNCTION MODEL FOR SINGLE QUANTUM WELL

The $k \cdot p$ model can be further applied to the quantum wells, which is already discussed in previous works [11,13,42]. We will briefly discuss here for reference.

The four-band $k \cdot p$ Hamiltonian describing the electronic structure of IV-VI quantum wells in the basis $|L_6^+, \uparrow\rangle$, $|L_6^+, \downarrow\rangle$, $|L_6^-, \uparrow\rangle$, $|L_6^-, \downarrow\rangle$ is written as follows:

$$\hat{H} = \begin{pmatrix} V_-(z) & 0 & -i\hbar v_z \partial_z & 0 \\ 0 & V_-(z) & 0 & i\hbar v_z \partial_z \\ -i\hbar v_z \partial_z & 0 & -2|\Delta| + V_+(z) & 0 \\ 0 & i\hbar v_z \partial_z & 0 & -2|\Delta| + V_+(z) \end{pmatrix}.$$

Here, $V_\pm$ represents the band offset at the interfaces ($z = 0$ and $z = L$). $V_\pm(z) = \pm V$ outside the well and 0 inside it (V is much larger than 2Δ). $-2|\Delta|$ is the position of the valence band edge, with the conduction band edge in the well taken to be at 0 (see Fig. 6).

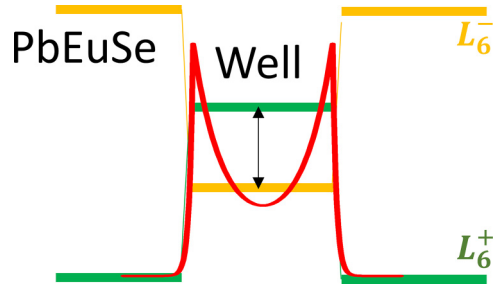

FIG. 6. Band diagram of the quantum well.

The detailed solution using envelope functions can be found in the references above. The result for $-2\Delta < E < 0$ is

$$\tanh\left(\frac{\kappa d}{2}\right) = -\frac{\rho(E + 2\Delta)}{\kappa(E + 2\Delta - V)}, \quad \text{even case},$$

$$\coth\left(\frac{\kappa d}{2}\right) = -\frac{\rho(E + 2\Delta)}{\kappa(E + 2\Delta - V)}, \quad \text{odd case}.$$

Here $\kappa = -\frac{1}{\hbar v_z}\sqrt{-E(E + 2|\Delta|}$. For sample S1, $d = 50$ nm, $2\Delta = 70$ meV (gap of bulk $Pb_{0.73}Sn_{0.27}Se$), $v_z = 4.36 \times 10^5$ m/s, and we take the gap of $Pb_{0.80}Eu_{0.20}Se$ to be $V = 750$ meV [43]. We can calculate the gap of TIS, S1, and S2 shown in Table I.

APPENDIX C: SPIN SPLITTING OF THE TOPOLOGICAL SURFACE STATE

Landau levels can be numerically solved by introducing perturbation Hamiltonian

$$H_{mn}^{\text{eff}}(B) = \int_{-\infty}^{\infty} dz \langle \vec{\Psi}_m | \Delta H | \vec{\Psi}_n \rangle,$$

where

$$\Delta H = \begin{pmatrix} -(N-1)\hbar\tilde{\omega}_c & 0 & 0 & \sqrt{2e\hbar v_c^2 BN} \\ 0 & -(N+1)\hbar\tilde{\omega}_c & \sqrt{2e\hbar v_c^2 BN} & 0 \\ 0 & \sqrt{2e\hbar v_c^2 BN} & -(N-1)\hbar\tilde{\omega}_v & 0 \\ \sqrt{2e\hbar v_c^2 BN} & 0 & 0 & -(N+1)\hbar\tilde{\omega}_v \end{pmatrix}.$$

Here we already take the approximation $\tilde{g}_{c,v}\mu_B B \approx \hbar\tilde{\omega}_{c,v}$. For the TSS state, the wave function is mixed, which means $|F_1^{\text{TSS}}|^2 = |F_2^{\text{TSS}}|^2$. The effective Hamiltonian then becomes $H_{ii}^{\text{eff}}(B) = \int_{-\infty}^{\infty} dz \langle \vec{\Psi}_i | \Delta H | \vec{\Psi}_i \rangle = -(N \pm 1)\hbar(\tilde{\omega}_c + \tilde{\omega}_v)/2$. In bulk, previous work has treated $|\tilde{\omega}_c| \approx |\tilde{\omega}_v|$. If we set them equal to each, the far-band corrections for the TSS will be zero. We thus define $\tilde{\omega}_{\text{eff}} = \frac{\tilde{\omega}_c + \tilde{\omega}_v}{2}$ and $\tilde{g}_{\text{eff}}\mu_B B \approx \hbar\tilde{\omega}_{\text{eff}}$. These terms require electron-hole asymmetry to be finite. The corresponding $H^{\text{eff}}(B)$ describing surface states then looks like the bulk one [44]. In practice, we find that the result is well described by the empirical equation:

$$E_i^{N,(\uparrow,\downarrow)} = \pm\hbar\tilde{\omega}_{\text{eff}} \pm \sqrt{(\Delta_i - N\hbar\tilde{\omega}_{\text{eff}})^2 + 2e\hbar N v_c^2 B},$$

$$\tilde{\omega}_{\text{eff}} = \frac{eB}{\tilde{m}_{\text{eff}}}.$$

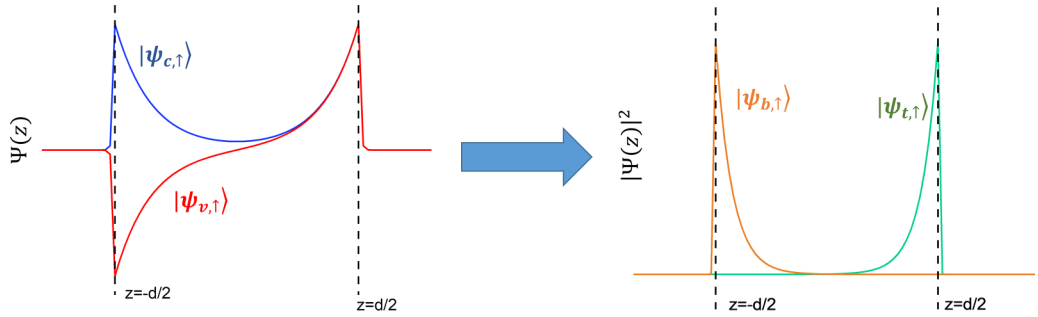

FIG. 7. A sketch showing the parity and probability distribution of different states. Left: The wave function of $|\psi_{c,\uparrow}\rangle, |\psi_{v,\uparrow}\rangle$ along z direction. To show they have opposite parity we are not plotting $|\Psi(z)|^2$. Right: Probability distribution of new basis $|\psi_t\uparrow\rangle$, $|\psi_b\uparrow\rangle$.

$\tilde{m}_{\text{eff}}$ can be estimated theoretically, by taking $\tilde{m}_c = 0.23 \pm 0.06 m_0$, $\tilde{m}_v = -0.115 \pm 0.03$ from Bauer [10]. We find $|\tilde{m}_{\text{eff}}| = 0.23 \pm 0.19$. Our own measurement of $|\tilde{m}_{\text{eff}}|$ falls in this range, as shown in the main text.

APPENDIX D: ORIGIN OF THE SPIN SPLIT

In this section we would like to relate our result to the common model used in TIs. Following the discussion in Appendixes B and C we can get the eigenstates $|\psi_{c,\uparrow}\rangle, |\psi_{c,\downarrow}\rangle$, $|\psi_{v,\uparrow}\rangle, |\psi_{v,\downarrow}\rangle$, which represent spin-up or spin-down eigenstates in conduction/valence bands. They can be rewritten as the symmetric and antisymmetric linear combination of states on the top $|\psi_t\uparrow\rangle$, $|\psi_t\downarrow\rangle$ and bottom $|\psi_b\uparrow\rangle$, $|\psi_b\downarrow\rangle$ surface. If we change the basis back, e.g., $|\psi_{t,b}\uparrow\rangle = (|\psi_{c,\uparrow}\rangle \pm |\psi_{v,\uparrow}\rangle)/\sqrt{2}$, $|\psi_{t,b}\downarrow\rangle = (|\psi_{c,\downarrow}\rangle \pm |\psi_{v,\downarrow}\rangle)/\sqrt{2}$, the effective Hamiltonian is

$$H = \begin{pmatrix} 0 & \sqrt{2e\hbar v_c^2 BN} & -(N-1)\hbar\tilde{\omega} & 0 \\ \sqrt{2e\hbar v_c^2 BN} & 0 & 0 & -(N+1)\hbar\tilde{\omega} \\ -(N-1)\hbar\tilde{\omega} & 0 & 0 & -\sqrt{2e\hbar v_c^2 BN} \\ 0 & -(N+1)\hbar\tilde{\omega} & -\sqrt{2e\hbar v_c^2 BN} & 0 \end{pmatrix}.$$

The Hamiltonian has a similar form as the Hamiltonian of four Dirac-type surface states [45,46]. The square root term comes from performing the ladder operator to the $\hbar v k_\pm$ term. The eigenenergy is solved to be

$$E(N) = \pm\hbar\tilde{\omega} \pm \sqrt{\hbar^2\tilde{\omega}^2 N^2 + 2e\hbar v_c^2 BN}.$$

When the field is zero, the states from the top and bottom surface are Kramers' partners [15].

In our original basis, $|\psi_{c,\uparrow}\rangle, |\psi_{v,\uparrow}\rangle$ have opposite parity. Their symmetric and antisymmetric combinations naturally lead to $|\psi_t\uparrow\rangle$, $|\psi_b\uparrow\rangle$ that lie on separate surfaces, as shown in Fig. 7. As the field goes up, these states get mixed because of the $-(N\pm1)\hbar\tilde{\omega}$ term in the Hamiltonian. As a result the mixed basis $|\psi_{c,\uparrow\downarrow}\rangle, |\psi_{v,\uparrow\downarrow}\rangle$ is more commonly used.

[1] L. Fu, Topological Crystalline Insulators, Phys. Rev. Lett. **106**, 106802 (2011).

[2] T. H. Hsieh, H. Lin, J. Liu, W. Duan, A. Bansil, and L. Fu, Topological crystalline insulators in the SnTe material class, Nat. Commun. **3**, 982 (2012).

[3] P. Dziawa, B. J. Kowalski, K. Dybko, R. Buczko, A. Szczerbakow, M. Szot, E. Łusakowska, T. Balasubramanian, B. M. Wojek, M. H. Berntsen, O. Tjernberg, and T. Story, Topological crystalline insulator states in $Pb_{1-x}Sn_xSe$, Nat. Mater. **11**, 1023 (2012).

[4] X. Li, F. Zhang, and A. H. MacDonald, Su (3) Quantum Hall Ferromagnetism in SnTe, Phys. Rev. Lett. **116**, 026803 (2016).

[5] C. Fang, M. J. Gilbert, and B. A. Bernevig, Large-Chern-Number Quantum Anomalous Hall Effect in Thin-Film Topological Crystalline Insulators, Phys. Rev. Lett. **112**, 046801 (2014).

[6] I. Sodemann, Z. Zhu, and L. Fu, Quantum Hall Ferroelectrics and Nematics in Multivalley Systems, Phys. Rev. X **7**, 041068 (2017).

[7] B. A. Assaf, T. Phuphachong, E. Kampert, V. V. Volobuev, P. S. Mandal, J. Sánchez-Barriga, O. Rader, G. Bauer, G. Springholz, L. A. de Vaulchier, and Y. Guldner, Negative Longitudinal Magnetoresistance from the Anomalous N = 0 Landau Level in Topological Materials, Phys. Rev. Lett. **119**, 106602 (2017).

[8] C. Zhang, Y. Liu, X. Yuan, W. Wang, S. Liang, and F. Xiu, Highly tunable berry phase and ambipolar field effect in topological crystalline insulator $Pb_{1-x}Sn_xSe$, Nano. Lett. **15**, 2161 (2015).

[9] A. Kazakov, W. Brzezicki, T. Hyart, B. Turowski, J. Polaczyński, Z. Adamus, M. Aleszkiewicz, T. Wojciechowski, J. Z. Domagala, O. Caha, A. Varykhalov, G. Springholz, T.

Wojtowicz, V. V. Volobuev, and T. Dietl, Signatures of dephasing by mirror-symmetry breaking in weak-antilocalization magnetoresistance across the topological transition in $Pb_{1-x}Sn_xSe$, Phys. Rev. B **103**, 245307 (2021).

[10] G. Bauer, Magnetooptical Properties of IV–VI Compounds, in *Narrow Gap Semiconductors Physics and Applications* (Springer, Berlin, 1980), Vol. 133, pp. 427–446.

[11] G. Krizman, B. A. Assaf, T. Phuphachong, G. Bauer, G. Springholz, L. A. de Vaulchier, and Y. Guldner, Dirac parameters and topological phase diagram of $Pb_{1-x}Sn_xSe$ from magnetospectroscopy, Phys. Rev. B **98**, 245202 (2018).

[12] C. M. Polley, V. Jovic, T.-Y. Su, M. Saghir, D. Newby, Jr., B. J. Kowalski, R. Jakiela, A. Barcz, M. Guziewicz, T. Balasubramanian, G. Balakrishnan, J. Laverock, and K. E. Smith, Observation of surface states on heavily indium-doped SnTe(111), a superconducting topological crystalline insulator, Phys. Rev. B **93**, 075132 (2016).

[13] Jiashu Wang, X. Liu, C. Bunker, L. Riney, B. Qing, S. K. Bac, M. Zhukovskyi, T. Orlova, S. Rouvimov, M. Dobrowolska, J. K. Furdyna, and B. A. Assaf, Weak antilocalization beyond the fully diffusive regime in $Pb_{1-x}Sn_xSe$ topological quantum wells, Phys. Rev. B **102**, 155307 (2020).

[14] J. Melngailis, T. C. Harman, and W. C. Kernan, Shubnikov-de haas measurements in $Pb_{1-x}Sn_xSe$, Phys. Rev. B **5**, 2250 (1972).

[15] Y.-S. Fu, T. Hanaguri, K. Igarashi, M. Kawamura, M. S. Bahramy, and T. Sasagawa, Observation of zeeman effect in topological surface state with distinct material dependence, Nat. Commun. **7**, 10829 (2016).

[16] Z. Zhang, W. Wei, F. Yang, Z. Zhu, M. Guo, Y. Feng, D. Yu, M. Yao, N. Harrison, R. McDonald, Y. Zhang, D. Guan, D. Qian, J. Jia, and Y. Wang, Zeeman effect of the topological surface states revealed by quantum oscillations up to 91 tesla, Phys. Rev. B **92**, 235402 (2015).

[17] A. A. Taskin and Y. Ando, Berry phase of nonideal dirac fermions in topological insulators, Phys. Rev. B **84**, 035301 (2011).

[18] J. Xiong, Y. Luo, Y. Khoo, S. Jia, R. J. Cava, and N. P. Ong, High-field shubnikov–de haas oscillations in the topological insulator Bi_2Te_2Se, Phys. Rev. B **86**, 045314 (2012).

[19] J. G. Analytis, R. D. McDonald, S. C. Riggs, J.-H. Chu, G. S. Boebinger, and I. R. Fisher, Two-dimensional surface state in the quantum limit of a topological insulator, Nat. Phys. **6**, 960 (2010).

[20] R. Winkler, *Spin-Orbit Coupling Effects in Two-Dimensional Electron and Hole Systems* (Springer, Berlin, 2003).

[21] G. Krizman, B. A. Assaf, G. Bauer, G. Springholz, L. A. de Vaulchier, and Y. Guldner, Miniband engineering and topological phase transitions in topological-insulator–normal-insulator superlattices, Phys. Rev. B **103**, 235302 (2021).

[22] G. Bastard, *Wave Mechanics Applied to Semiconductor Heterostructures* (Wiley-Interscience, New York, 1991).

[23] T. Phuphachong, B. Assaf, V. Volobuev, G. Bauer, G. Springholz, L.-A. de Vaulchier, and Y. Guldner, Dirac landau level spectroscopy in $Pb_{1-x}Sn_xSe$ and $Pb_{1-x}Sn_xTe$ across the topological phase transition: A review, Crystals (Basel) **7**, 29 (2017).

[24] G. Bauer, H. Pascher, and W. Zawadzki, Magneto-optical properties of semimagnetic lead chalcogenides, Semicond. Sci. Technol. **7**, 703 (1992).

[25] G. Krizman, B. A. Assaf, T. Phuphachong, G. Bauer, G. Springholz, G. Bastard, R. Ferreira, L. A. de Vaulchier, and Y. Guldner, Tunable dirac interface states in topological superlattices, Phys. Rev. B **98**, 075303 (2018).

[26] H. Pascher, G. Bauer, and R. Grisar, Magnetooptical investigations and four-wave-mixing spectroscopy of PbSe, Phys. Rev. B **38**, 3383 (1988).

[27] G. Krizman, B. A. Assaf, M. Orlita, T. Phuphachong, G. Bauer, G. Springholz, G. Bastard, R. Ferreira, L. A. de Vaulchier, and Y. Guldner, Avoided level crossing at the magnetic field induced topological phase transition due to spin-orbital mixing, Phys. Rev. B **98**, 161202 (2018).

[28] H. Burkhard, G. Bauer, and W. Zawadzki, Band-population effects and intraband magneto-optical properties of a many-valley semiconductor: PbTe, Phys. Rev. B **19**, 5149 (1979).

[29] D. L. Mitchell and R. F. Wallis, Theoretical energy-band parameters for the lead salts, Phys. Rev. **151**, 581 (1966).

[30] B. A. Assaf, T. Phuphachong, V. V. Volobuev, G. Bauer, G. Springholz, L.-A. de Vaulchier, and Y. Guldner, Magnetooptical determination of a topological index, npj Quantum Mater. **2**, 26 (2017).

[31] N. Miura, *Physics of Semiconductors in High Magnetic Fields* (Oxford University Press, New York, 2007).

[32] M. S. Adler, C. R. Hewes, and S. D. Senturia, $K{\cdot}p$ Model for the magnetic energy levels in PbTe and $Pb_{1-x}Sn_xTe$, Phys. Rev. B **7**, 5186 (1973).

[33] C. K. N. Patel and R. E. Slusher, Electron spin-flip raman scattering in PbTe, Phys. Rev. **177**, 1200 (1969).

[34] Y. Jiang, M. Ermolaev, G. Kipshidze, S. Moon, M. Ozerov, D. Smirnov, Z. Jiang, and S. Suchalkin, Giant G-factors and fully spin-polarized states in metamorphic short-period InAsSb/InSb superlattices, Nat. Commun. **13**, 5960 (2022).

[35] A. R. Calawa, J. O. Dimmock, T. C. Harman, and I. Melngailis, Magnetic Field Dependence of Laser Emission in $Pb_{1-x}Sn_xSe$ Diodes, Phys. Rev. Lett. **23**, 7 (1969).

[36] P. Kästner and G. Landwehr, Determination of the transverse G-factors for n- and p-Type PbSe by magnetoacoustic quantum oscillations, Phys. Status Solidi **41**, K71 (1970).

[37] R. Xiao, J. Zhang, J. Chamorro, J. Kim, T. M. McQueen, D. Vanderbilt, M. Kayyalha, Y. Li, and N. Samarth, Integer Quantum hall effect and enhanced g factor in quantum-confined Cd_3As_2 films, Phys. Rev. B **106**, L201101 (2022).

[38] L. M. Roth, B. Lax, and S. Zwerdling, Theory of optical magneto-absorption effects in semiconductors, Phys. Rev. **114**, 90 (1959).

[39] J. Yuan, M. Hatefipour, B. A. Magill, W. Mayer, M. C. Dartiailh, K. Sardashti, K. S. Wickramasinghe, G. A. Khodaparast, Y. H. Matsuda, Y. Kohama, Z. Yang, S. Thapa, C. J. Stanton, and J. Shabani, Experimental measurements of effective mass in near-surface InAs quantum wells, Phys. Rev. B **101**, 205310 (2020).

[40] X. C. Zhang, K. Ortner, A. Pfeuffer-Jeschke, C. R. Becker, and G. Landwehr, Effective g factor of N-Type $HgTe/Hg_{1-x}Cd_xTe$ single quantum wells, Phys. Rev. B **69**, 115340 (2004).

[41] R. L. Bernick and L. Kleinman, Energy bands, effective masses and g-factors of the lead salts and SnTe, Solid State Commun. **8**, 569 (1970).

[42] J. Wang, T. Wang, M. Ozerov, Z. Zhang, S.-K. Bac, H. Trinh, M. Zhukovskyi, T. Orlova, H. Ambaye, J. Keum, D. Smirnov, V. Lauter, X. Liu, and B. A. Assaf, Magnetic

proximity-induced energy gap of topological surface states, arXiv:2207.07685.

[43] M. Simma, G. Bauer, and G. Springholz, Temperature Dependent Band Offsets in PbSe/PbEuSe Quantum Well Heterostructures, Appl. Phys. Lett. **101**, 172106 (2012).

[44] G. Krizman, *Étude Magnéto-Optique Des Transitions de Phase Topologique Dans Les Alliages* $Pb_{1-x}Sn_xSe$ *et Leurs Hétérostructures* (Ecole Normale Supérieure, Paris Sciences et Lettres, Paris, 2020).

[45] R. Yu, W. Zhang, H. J. Zhang, S. C. Zhang, X. Dai, and Z. Fang, Quantized anomalous hall effect in magnetic topological insulators, Science **329**, 61 (2010).

[46] X. L. Qi and S. C. Zhang, Topological insulators and superconductors, Rev. Mod. Phys. **83**, 1057 (2011).